ACS APPLIED NANO MATERIALS

www.acsanm.org Article

Low-Defect Laser-Induced Graphene from Lignin for Smart Triboelectric Touch Sensors

Shuhong Yang, Bujingda Zheng, Honghua Qian, Qiangu Yan, Guoliang Huang, Jian Lin, and Caixia Wan*

Cite This: *ACS Appl. Nano Mater.* 2024, 7, 25241−25248 Read Online

ACCESS | Metrics & More | Article Recommendations | Supporting Information

ABSTRACT: Laser-induced graphene (LIG) has emerged as a versatile carbon material for broad applications. However, the synthesis of high-quality LIG materials, especially with low defects, remains underexplored. This study was thus focused on developing a facile and cost-effective alternative to producing low-defect LIG, especially using lignin as a renewable precursor. The results showed that lignin treated by methyl ethyl ketone yielded LIG with a markedly low-defect level (I_D/I_G ratio of 0.12) by direct laser writing under ambient conditions. The triboelectric tactile sensor fabricated from low-defect LIG electrodes exhibited exceptional durability (over 15,000 cycles), accurate and real-time responsiveness (<0.01 s), wide-ranged touch frequencies (1−6 Hz), and ultrasensitivity to pressure (5−300 kPa). Moreover, the sensor was successfully demonstrated for the wireless control of LEDs. This work indicated that lignin-derived low-defect LIG has great potential for smart electronics applications.

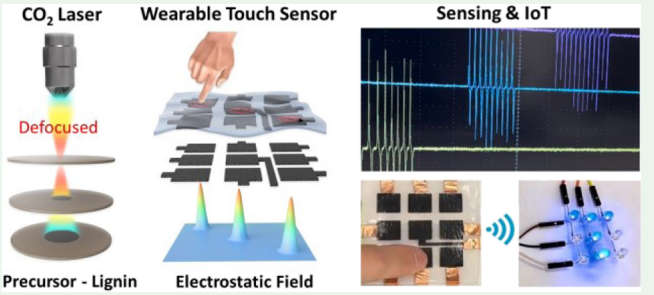

KEYWORDS: *direct laser writing, laser-induced graphene, lignin, low defects, triboelectric touch sensors*

INTRODUCTION

Laser-induced graphene (LIG) has emerged as a promising carbon material due to its excellent features including high electrical conductivity, mechanical flexibility, thermal stability, chemical resistance, and high specific surface area.[1] Direct laser writing (DLW) for LIG synthesis features a single-step, maskless, and rapid process, addressing the limitations of conventional techniques (e.g., chemical vapor deposition and Hummers' method) in the mass production of low-cost graphene materials, especially via roll-to-roll manufacturing.[2] Both synthetic polymers [e.g., polyimide (PI)] and renewable materials (e.g., wood, leaves) have been explored as substrates/precursors for LIG synthesis.[3−7] Among various precursors, lignin stands out given its high carbon contents and abundant aromatic rings favorable for the formation of higher-quality LIG [e.g., relatively low sheet resistance (R_s) of 5−10 Ω sq^{-1}] (Table S1).[7−11] Moreover, compared to raw biomass/lignocellulosic biomass, lignin can be processed in the form of film with high uniformity and good consistency that are suited to DLW.[6,9,12] Lignin-derived LIG has also shown impressive performance in sensing and supercapacitor applications.[13] However, despite diverse sources and intriguing attributes, LIG still has noticeable defects compared with pristine graphene. Defects in LIG should be minimized especially when targeting electronic applications that need high electrical or thermal conductivity.[14,15]

Wearable tactile sensors have attracted much attention due to their high compatibility with human−machine interface (HMI) and Internet of Things (IoT) applications (e.g., healthcare devices, robotics interfaces, and virtual reality systems).[16−18] Conventional tactile sensors based on capacitive and piezoelectric principles have several drawbacks including slow response time, lack of flexibility, bulkiness, and high fabrication cost.[19−22] Triboelectric tactile sensors present a promising approach to addressing those drawbacks given their simultaneous tactile sensing and energy harvesting functions.[23] Such sensors can be configured in a cost-effective and compact way, especially by incorporating emerging electrode materials with high conductivity, high surface area, and lightweight rather than conventional metal electrodes (e.g., aluminum and copper). LIG is emerging as a new class of conductive materials and its adoption as triboelectric electrode materials would promote the development of next-generation HMI and IoT devices.[24−26] Moreover, by reducing defects in LIG, it is highly promising to develop high-performance induction electrodes with fast response, high sensitivity, lightweight, and low cost. Overall, exploiting LIG as active materials for triboelectric induction electrodes will advance the development of tactile sensors and

Received: September 18, 2024
Revised: October 10, 2024
Accepted: October 14, 2024
Published: October 30, 2024

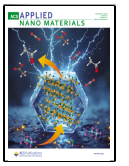

https://doi.org/10.1021/acsanm.4c05362
ACS Appl. Nano Mater. 2024, 7, 25241−25248

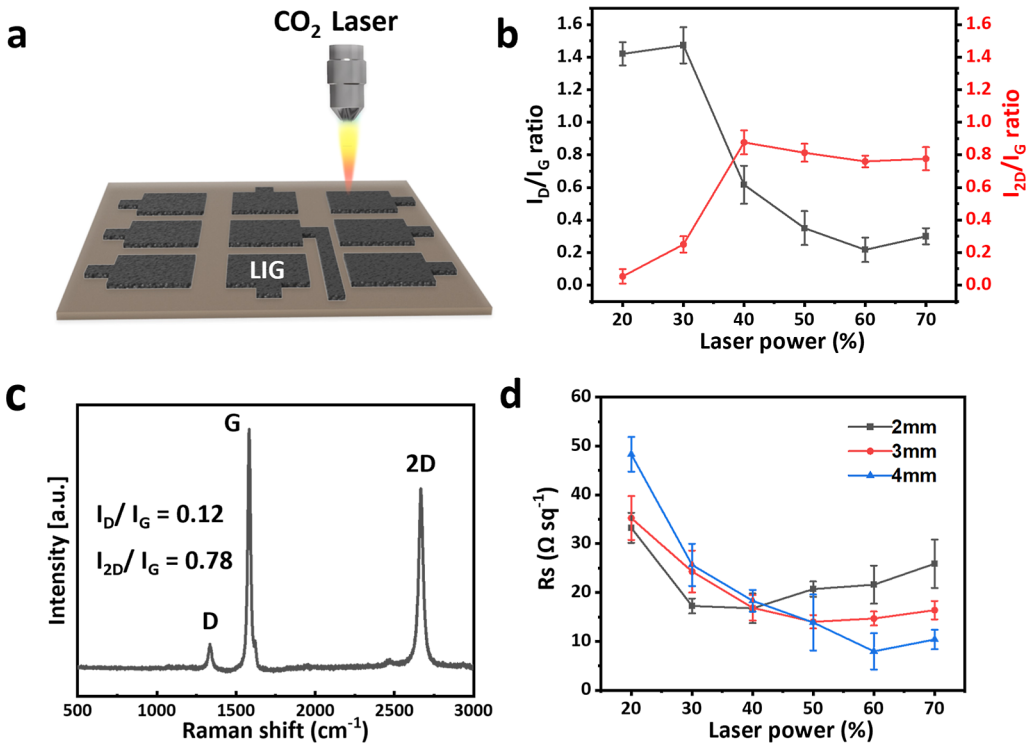

Figure 1. LIG characteristics. (a) Schematic model of developing lignin-derived LIG using CO_2 laser. (b) I_D/I_G and I_{2D}/I_G for LIG at 4 mm defocus distance. (c) Raman spectrum of L60D4, showing the lowest I_D/I_G of 0.12. (d) R_s of LIG samples. Defocus distances: 2-, 3-, and 4 mm. Average values and error bars are based on 10 independent measurements.

their applications in various fields such as energy harvesting, manufacturing, agriculture, and healthcare.[27−29]

The main objective of this study was to tailor a lignin-derived LIG with markedly low defects and high conductivity. Flexible and wearable tactile sensors based on electrodes patterned with low-defect LIG were fabricated for real-time tactile sensing with high performance. A smart wireless system based on a triboelectric sensor was also showcased for controlling LEDs on/off. The sensor demonstrated great potential for wearable and interactive electronics.

MATERIALS AND METHODS

Materials. Kraft lignin was kindly provided by the Domtar Corporation (Fort Mills, South Carolina, USA). Dragon Skin 10 MEDIUM was purchased from Smooth-On Inc. (Macungie, Pennsylvania, USA). All of the chemicals were purchased at Fisher Scientific (Hampton, New Hampshire, USA) and used as received.

LIG Synthesis. The lignin solution was prepared by dissolving kraft lignin in 95% methyl ethyl ketone (MEK) solution at a mass ratio of 1:3 with continuous mixing at room temperature for 24 h. Then, 4 g of lignin solution was first mixed with 10 g of 2 wt % NaOH solution at a mass ratio of 1:2.5, which was further added to 10 g of 9 wt % PVA (M_W 146,000−186,000) solution with continuous mixing to obtain a homogeneous dark brown liquid. The liquid was then poured into a plastic Petri dish (9 cm in diameter) and dried at 35 °C in an environmental chamber (25−50% humidity) for about 30 h until it reached a constant weight. Thereafter, the lignin film was removed from the Petri dish and attached to a glass slide by using an adhesive tape.

The DLW process was carried out using a CO_2 laser (Universal Laser Systems VLS3.50 Laser Cutter/Engraver, Scottsdale, Arizona, USA) under ambient conditions with 1000 pulses per inch, 10% speed, different defocus distances (2.0, 3.0, and 4.0 mm), and different power levels (20−70% with 10% increment). The laser power output (W) was measured by an AA30 Astral laser power meter (Boulder, Colorado, USA). LIG samples were labeled as LxDy, where x stands for laser power level (%) and y stands for defocus distance (mm).

Fabrication of Triboelectric Tactile Sensors. The LIG electrodes with 3 × 3 arrays were fabricated into a triboelectric tactile sensor as follows. First, Dragon Skin, a mixture of Polymers A (silicone) and B (curing agent) (1:1, w/w), was applied to the top layer of LIG electrodes with 0.5 mm thickness at a spinning rate of 300 rpm and an acceleration rate of 300 rpm/s by using a spin coater (Model WS-650MZ-23NPPB, Laurell Technologies, Lansdale, Pennsylvania, USA). After curing LIG-Dragon Skin in a convection oven at 35 °C for 30 min, the film was submerged in deionized water for about 10 min to allow the complete detachment of the LIG-Dragon Skin composite from the lignin film that remained uncarbonized via a so-called water lift technique as reported in our prior study.[10] Copper tape was then affixed to each end of the LIG electrode using conductive silver paint. After air drying, the LIG-Dragon Skin composite (uncoated side) was applied with Dragon Skin with 0.5- and 1.5 mm thickness at a fixed acceleration rate of 100 rpm/s while controlling the spinning speed rates at 100 and 300 rpm, respectively. The final device assembly was cured at 35 °C in a convection oven for 30 min and then cut into 5 × 5 cm for sensing testing.

Characterization. Raman spectra of LIG were acquired on an inVia confocal Raman microscope (Renishaw, West Dundee, Illinois, USA) at 633 nm. Scanning electron microscopy (SEM) images were acquired on a FEI Quanta 600 FE-SEM (FEI company, Hillsboro, Oregon, USA) operated at 15 kV and 100 pA. For SEM imaging, LIG embedded in the lignin films were imaged directly, while the lignin film itself was coated with 25 μm of platinum by a Quorum 150TES Sputter Coater (Quorum Technologies Ltd., East Sussex, UK). High-resolution transmission electron microscopy (HRTEM) images were acquired on a ThermoScientific Spectra 300 microscope operated at 300 kV. The LIG powder scraped from the scribed lignin film was sonicated in ethanol for 10 min and used for HRTEM imaging. R_s was measured by Pro-4 Four Point Resistivity Systems (Lucas Laboratories, Gilroy, California, USA).

Electrical Measurement. For the triboelectric tactile sensors, the open-circuit voltage (V_{oc}) generated by one LIG electrode was

https://doi.org/10.1021/acsanm.4c05362
ACS Appl. Nano Mater. 2024, 7, 25241−25248

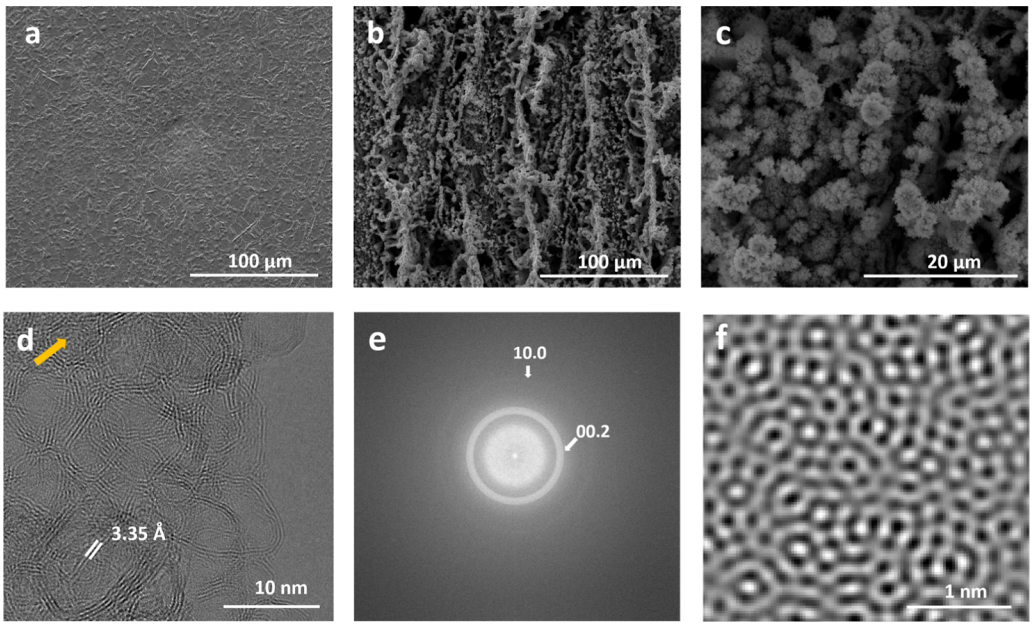

Figure 2. SEM and TEM images. (a) SEM image of the lignin film (scale bar: 100 μm). (b) SEM image of L60D4 (scale bar: 100 μm). (c) SEM image of L60D4 (scale bar: 20 μm). (d) HRTEM image of L60D4 (scale bar: 10 nm). (e) 2D-FFT image of L60D4. (f) Cs-STEM image at the area indicated in Figure 2d (yellow arrow) (scale bar: 1 nm).

measured by using an oscilloscope (DPO4034, Tektronix, Beaverton, Oregon, USA). A multimeter (Keithley DAQ6510, Tektronix, Beaverton, Oregon, USA) was used for output current measurement when one LIG electrode (0.8 × 0.8 cm) was working as a triboelectric nanogenerator for energy harvesting, with commercial ceramic resistors connected in series to one LIG electrode as external loads (1.5 kΩ−100 MΩ), with ∼6 N and 4 Hz finger touch applied consistently. The periodical contact/separation cycles for durability testing were controlled by a vibrating shaker motor (Permanent Magnet Shaker LDS (B&K V203), Bruel & Kjaer, Duluth, Georgia, USA), with one finger fixed at the same position while vibrating the sensor at 50 Hz with 0.5 cm shaking amplitude. A Digital Toploading Balance (Denver Instrument TR-4102D, American laboratory Trading, East Lyme, Connecticut, USA) was used to generate force reading. Pressure was calculated when the actual touch was controlled to 0.2 cm^2. In the LED wireless control system, a multiplexer was first used to detect tactile signals (V_{oc}) by linking its multichannels separately with individual electrodes (3 × 3 arrays). The detected signals were then transferred to the first microcontroller (Arduino Mega 2560 R3, Boston, Massachusetts, USA) for processing. Once processed, the signals were transmitted wirelessly by two RF modules (NRF24L01, HiLetgo, Shenzhen, Guangdong, China) in series. Another microcontroller (Arduino Mega 2560 R3) responsible for receiving those transmitted signals was used to control the LEDs on/off.

RESULTS AND DISCUSSION

LIG Characteristics. Laser power and defocus distance are two important parameters (Figure 1a). Especially, by adjusting a laser focal point either above or below a laser focal plane, a substrate can be treated more uniformly under broader exposure to photothermal energy (Figure S1a).[30] In this work, three defocus distances (2, 3, and 4 mm) along with five laser power levels (20%−70%, 10% increment) were investigated, with corresponding laser power output (W) measured (Figure S1b). All of the LIG samples and their characteristics are summarized in Table S2. The Raman spectra of LIG showed three prominent peaks (Figure S2): D (∼1360 cm^{-1} indicating defects and distortion in the sp^2 carbon bonds), G (∼1580 cm^{-1} arising from the first-order band of all sp^2 hybridized bonds), and 2D peaks (∼2670 cm^{-1} derived from second-order zone boundary phonons).[31] A lower I_D/I_G ratio suggested a lower level of defects in graphene. At 2 mm defocus distance, the defect levels of LIG decreased first when increasing the power level from 20% to 50% and then increased when further increasing the laser power level. In contrast, at 3- and 4 mm defocus distances, the power level above 50% still led to low-defect LIG (Figure S2b,c). Such a trend was also reflected in the R_s change (Figure 1b). Notably, a markedly low I_D/I_G ratio of 0.12 was achieved in L60D4 (Figure 1c). The findings suggested that increasing the laser defocus distance could mitigate thermal damage and defects in LIG caused by high power. The synergistic effects of defocus distance and laser power resulted in high-quality LIG with minor defects. To the best of our knowledge, this is the lowest I_D/I_G ratio reported so far.[5,32−35] In addition to the laser parameters, treating lignin with MEK was beneficial for LIG quality. In such an organic solvent, lignin chains can be reconfigured and become more extended, which could make aromatic rings and carbon atoms more available for graphene synthesis, resulting in lower defects and improved crystallinity in LIGs.[3,5,10,35−38] It was interesting to note that LIG derived from kraft lignin showed the best quality compared to the counterparts derived from alkaline lignin and organosolv lignin (Table S3). This finding suggested that the optimal solvent system and lasing condition should be precursor-specific, and further optimization should be necessary for other types of technical lignin.

LIG morphological changes were examined by SEM imaging. When increasing the laser power level from 20% to 70% at 4 mm defocus distance (corresponding to measured 0.63−2.1 W of laser power output), LIG retained a similar structure as evidenced by consistent visible laser traces (Figure S3). Interestingly, more microspheres were formed within the LIG porous matrix when increasing the laser power. Such a microsphere formation was not noticeable in the LIG induced from the lignin film made of the alkaline lignin solution reported in our prior study.[10] The sizes of those microspheres remained

https://doi.org/10.1021/acsanm.4c05362
ACS Appl. Nano Mater. 2024, 7, 25241−25248

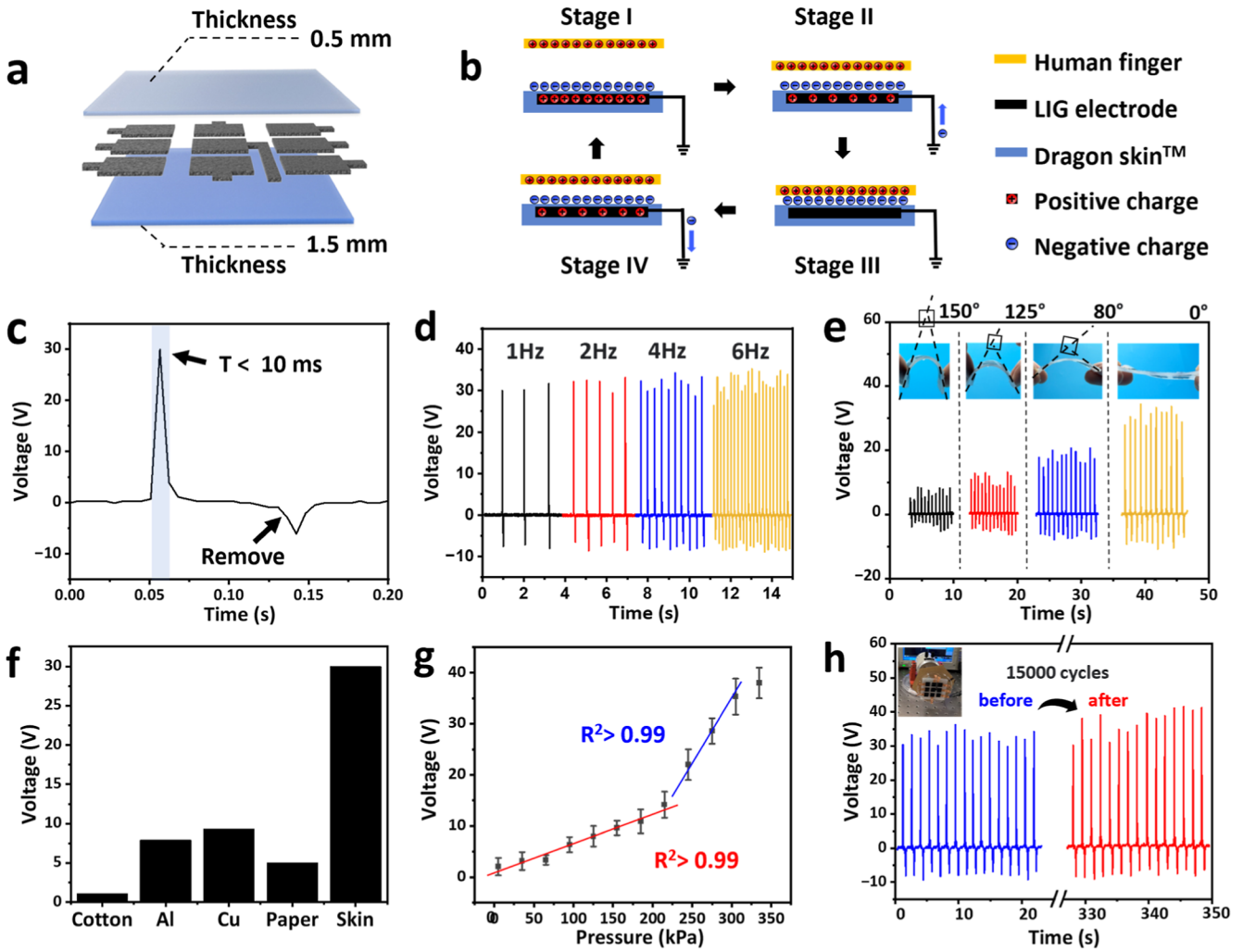

Figure 3. Sensing performance of the triboelectric touch sensor fabricated from L60D4. (a) Schematic model of the triboelectric touch sensor. (b) Illustration of the charge distribution within a single sensor unit during a touch-separate cycle between a human finger and the touch sensor. (c) V_{oc} signals with respect to the response time during a single touch-separate cycle, with ∼6 N and 4 Hz touch. (d) V_{oc} variation in response to different finger touch frequencies, with ∼6 N touch. (e) V_{oc} at varying bending angles: 0°, 80°, 125°, and 150°, with ∼6 N and 2 Hz touch. (f) V_{oc} in response to different materials, with ∼6 N and 6 Hz touch, corresponding to surface potential signals (Figure S7). (g) V_{oc} with average values calculated from five independently repeated signals when exposing one LIG electrode to the pressure of 5−300 kPa. (h) Generated V_{oc} signals with ∼6 N and 1 Hz touch before and after 15,000 touch-separate finger touch cycles simulated by 50 Hz vibration.

relatively consistent (1−2 μm in diameter) even at 70% laser power. These findings suggested that a proper solvent would enable more controllable carbonization and graphitization during laser irradiation, resulting in relatively uniform microspheres and consistent surface morphology even under more powerful laser irradiation.

The low-defect L60D4 was further examined for its ultrastructures. HRTEM revealed the fringe-like patterns with a measured *d*-spacing of 0.355 nm between adjacent (002) planes in the graphitic carbon structure (Figure 2d). Figure 2e shows the ring-shaped pattern in the 2D fast Fourier transform (2D-FFT) mode. The outer ring 10.0 corresponded to the basal plane of graphite, while the inner circle ring 0.02 indicated that folded multilayers of graphene were formed.[5] In Figure 2f, the aberration-corrected scanning TEM (Cs-STEM) image showed the ultrapolycrystalline feature of LIG flakes with disordered-grain boundaries in a moiré pattern, suggesting the formation of rotational stacking of multilayer graphene (i.e., 2−6 layers). These results indicated that the graphene layers were randomly oriented, and the stacking layers formed a turbostratic structure.[39] Considering intriguing characteristics especially with well-defined graphene domains and low defects, L60D4 was further explored as working electrodes for triboelectric tactile sensing as discussed in the latter section.[39]

Sensor Performance. The schematic assembly of the sensor is illustrated in Figure 3a. As described above, the touch sensor comprised a 3 × 3 sensing array (0.8 × 0.8 cm each square) of precisely laser-patterned L60D4 along with Dragon Skin (silicone) applied on both top and bottom sides of the LIG layer. Water lifting facilitated the completed LIG transfer from its original film substrate.[10] As a result, the LIG structure was well preserved after its transfer onto silicone (Figure S4). LIG itself is known to have high thermal stability and strong chemical resistance.[1] In addition, the sandwiched structure can benefit the LIG electrode by providing protective layers and maintaining its structural integrity. The functioning mechanism of one electrode in the touch sensor is illustrated in Figure 3b. The working principle was based on triboelectrification between the human finger and the silicone layer (top) coupled with the electrostatic induction between the silicone layer and con-

https://doi.org/10.1021/acsanm.4c05362
ACS Appl. Nano Mater. 2024, 7, 25241−25248

ductive LIG electrode. Frictional interactions between the human finger and silicone layer (top) led to the distribution of equal amounts of opposite charges on the respective surfaces (i.e., positive charges on skin and negative charges on the silicone surface) given their different triboelectric polarities. With opposite electrostatic fields formed in between, when the human finger was far away from the silicone layer (top) (Stage I), negative electrostatic field on the silicone surface would induce positive charges in the LIG electrode to the greatest extend. As the human skin moved back to, but not yet touched, the silicone layer (top) (Stage II), the positive electrostatic field on human finger started partially offset the effects of the silicone layer's electrostatic induction on the LIG electrode. This gradually altered the electrostatic environment around the LIG electrode. At the point of direct contact between the skin and silicone layer (Stage III), the electrostatic fields of the human finger and silicone layer completely offset each other's induction effects on the LIG electrode. Without being influenced by external electrostatic fields, the grounded LIG electrode subsequently lost all of the previously induced charges. In other words, the polarized condition inside the LIG disappeared. As the finger moved away from the top layer (Stage IV), the induction cycle happened again, resulting in gradual reinduction of positive charges in the LIG electrodes. The flow of electrons between the LIG electrode and the ground allowed an oscilloscope or semiconductor to capture V_{oc} or flowing current as signals.

For a triboelectric device, its key performance parameters include the generated peak value of V_{oc} as well as the current and power output when a load is connected. Specifically, it not only functions as a tactile sensor but also acts as an energy harvester when connected to capacitors or external loads. The sensor's voltage and current output characteristics were systematically studied. Our initial step involved tactile sensing with human finger touches. Figure 3c depicts the V_{oc} changes generated within one finger touch. Notably, the signal response time was less than 0.01 s, which was more than 10 times shorter than that of the state-of-the-art touch sensors (Table S4).[17] Such a rapid response could be attributed to the enhanced conductivity of low-defect graphene (L60D4). In contrast, the sensors fabricated by high-defect LIG (L30D4) (0.8 × 0.8 cm) generated a much weaker signal (only ∼10 V) with the same human touch (Figure S5). It was worth noting that such a peak V_{oc} value was achieved by one L60D4 electrode even with 0.1 × 0.1 cm (Figure S6), suggesting excellent efficiency of low-defect LIG in generating strong signals even at a tiny area for high-resolution sensing. These findings highlighted the great promise of low-defect LIG in sensing applications that demand a fast tactile feedback and strong signal feedback.

Human tactile touches are usually between 1 and 6 Hz. Remarkably, the sensor exhibited a fast and consistent response to touch with different frequencies (i.e., 1, 2, 4, and 6 Hz) (Figure 3d), peaking the V_{oc} value at ∼30 V. Owing to the flexibility of the elastomeric substrate, the sensor also worked effectively even under bending conditions. Figure 3e depicts the sensor's V_{oc} changes at various bending angles. When being flat, the sensor yielded a peak V_{oc} as high as 30 V. While being bent above 150°, the peak V_{oc} decreased to ∼10 V. This change could be explained by the fact that the generation of V_{oc} within the induction electrodes was closely associated with the contact area, electrical conductivity, and specific surface area of the electrodes. At no bending, the conductivity of the LIG-Dragon Skin composite was optimized due to good interconnection within the porous structures. At bending, the microcracks occurred within the LIG structure. Under excessive bending, the microcracks could lead to localized nonconductive gaps. Consequently, it decreased the effective area of the LIG electrode, compromising the V_{oc} peak value even when exposed to the same external stimulus. Notably, after cyclic bending and subsequent relaxation, the affected region of the LIG demonstrated excellent resilience. Repeatable V_{oc} values demonstrated that microcracks could effectively reconnect and reform the conductive pathways. These results showcased the LIG's exceptional stability and flexibility.

Other triboelectric materials such as cotton, metals (Cu and Al), and paper were also tested as touch materials, generating a V_{oc} value from 1 to 9.8 V (Figure 3f). As per the triboelectric series, the interaction with different materials resulted in varying surface charge densities and consequently led to different V_{oc} patterns (Figure S7). The signal pattern variations could be attributed to the distinct triboelectricities of these materials, either tending to gain or lose electrons during contact. The variability in response to different materials demonstrated the sensor's sensitivity and immense potential for precise object recognition applications.

To investigate the pressure sensitivity of the sensor, the V_{oc} was recorded while applying a touch with gradually increasing force. Notably, the V_{oc} exhibited two positive linear phases within the contact pressure range 0 to 300 kPa, including the first phase from 0 to 225 kPa and the second phase from 250 to 300 kPa (Figure 3g). Furthermore, 15,000 fast touch-separate cycles at 50 Hz were simulated by a vibrator while fixing the finger position. After such intense high-frequency touch, the sensor still generated consistent and stable V_{oc}, demonstrating the sensor's robustness and reliability (Figure 3h). To assess its dual function of one triboelectric electrode working as an energy harvester, we measured the current and power outputs of this single electrode under variable resistive loads. A peak power output of 20.3 μW, with a corresponding current of 2.6 μA, was recorded when the device was connected to an external resistor of 3 MΩ (Figure S8).

To further evaluate the sensor's performance as a wearable device, we affixed the sensor on a human arm and tested its responsiveness to both vertical and sliding touches. The sensor's real-time performance during actual wear (with 1.5 mm silicone bottom layer attached to arm) is demonstrated in Video S1 and Figure S9. The sensor worn on a human arm experienced a 10 V decrease in V_{oc} peak value compared to that attached to the stainless-steel surface for all the tests discussed above. This was attributed to different triboelectricities between two types of contact surfaces. Specifically, the silicone bottom layer would become negatively charged when in contact with human skin that has positive triboelectricity but remains uncharged when in contact with steel that has neutral triboelectricity. It should be noted that the negatively charged surface of the silicone bottom layer was insufficient to neutralize the positive electrostatic field of the human arm. The unneutralized positive field can consistently counteract electrostatic induction in LIG electrodes under touches on the top silicone layer. Subsequently, the V_{oc} peak value was significantly reduced. Nonetheless, the sensor still exhibited high sensitivity against touches with different frequencies and pressure. The real-time data, as shown in Videos S1, S2, demonstrated the sensor's remarkable efficiency in generating precise signal peaks against specific tactile stimuli.

Additionally, we found when the device was directly worn on the arm that the thickness of the bottom silicone layer played a

https://doi.org/10.1021/acsanm.4c05362
ACS Appl. Nano Mater. 2024, 7, 25241−25248

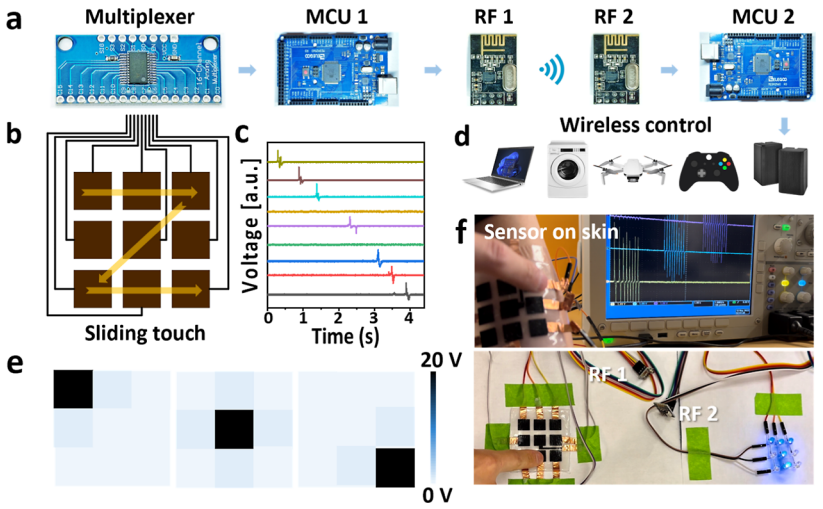

Figure 4. Wireless control system employing RF technology. (a) Illustration of a wireless control system employing RF modules. (b) Visualization of voltage signal generated during finger touch in a sliding mode, forming the letter "Z". (c) Output voltage generated by finger touch in a sliding mode, forming the letter "Z". (d) Demonstrating potential applications enabled by the wireless control system. (e) Visualization of the V_{oc} generated by a sensor attached to a human arm when applying touches from the upper left to the lower right. (f) Photo of the tactile sensor when attached to a human arm (top) and a photo of the LED wireless control system (bottom).

crucial role in ensuring tactile sensing performance. Specifically, we tested two thicknesses (0.5 vs 1.5 mm) for the bottom silicone layer while keeping the thickness of top silicone layer same (Figure S9). With the thin bottom layer, the V_{oc} peak value reached only 0.5 V, whereas with the thick bottom layer, the V_{oc} peak value reached as high as 20 V. This substantial difference could be attributed to the degree of electrostatic induction in the LIG electrodes sandwiched by two silicone layers. A thicker silicone bottom layer increased the distance from LIG electrodes to the bottom surface, which made induction in LIG electrode less affected by overall electrostatic fields from the bottom plane. The findings suggested that when the sensor was used as a wearable device on the human body, the thickness of the bottom silicone layer should be optimized for generating effective V_{oc} against touch stimuli on the top silicone layer.

Wireless Sensor toward IoT. Based on the excellent sensing performance, we further developed a wireless LED control system (Figure 4a). Each LIG electrode was connected to one of the channels in the multiplexer. In operation, when a human finger contacted the sensor, the multiplexer captured raw V_{oc} signals (Figure 4b,c). These signals were subsequently analyzed by a microcontroller unit (MCU) to generate command signals (Figure 4d). Figure 4e visualizes the V_{oc} generated by a sensor attached to a human arm when touche are applied from the upper left to the lower right. An algorithm was employed to set a threshold value in the MCU. In the setup, a V_{oc} exceeding 5 V would trigger the MCU to send command signals to RF Module 1. Actingas a receiver, RF Module 2 captured the wireless signals and forwarded them to another MCU. Then, the second MCU controlled LEDs on and off (Figure 4f). In Videos S3 and S4, we demonstrated how the LEDs were wirelessly controlled on/off. Vertical touches on each sensing unit could efficiently turn on the corresponding LED. The second click turned the LED off. Similarly, a sliding touch writing a letter "h" could also be mirrored by the LED display. The second sliding motion over the same locations turned off the activated LEDs. It is worthy to mention that the sensor used for wireless control as shown in Videos S3 and S4 was the exact same one used 2 weeks earlier for stability evaluation based on high-frequency contact as shown in Videos S1 and S2. Strikingly, the sensor showed no noticeable compromise in accuracy and stability of signals and well sustained functions for wireless control (Videos S3 and S4), indicating its reliability and robustness across multiple assessments and repeated uses. Overall, the sensor's capacity of wireless control and stability highlighted great promise of lignin-derived low-defect LIG as induction electrodes for smart electronic applications (e.g., robotics, human health monitoring, and environmental monitoring).

CONCLUSIONS

Low-defect laser induced graphene (LIG) with an unprecedentedly low I_D/I_G ratio of 0.12 was fabricated from MEK-treated kraft lignin under the optimized lasing conditions of 60% power level and 4 mm defocus distance. This low-defect LIG was used as induction electrodes for a triboelectric touch sensor. The sensor exhibited ultrafast real-time responsiveness (<0.01 s) across different touch frequencies (1−6 Hz) even with bending and exhibited ultrasensitivity to pressure ranging from 5 to 300 kPa. It also showcased exceptional durability after 15,000 touch-separate cycles. Furthermore, a smart wireless LED control system was developed and tested. Single touch or sliding gestures wirelessly controlled LED array on and off smoothly. This work highlighted the feasibility of cost-effective fabrication of low-defect LIG and great promise of such high-quality LIG for its adaptability and performance in smart electronics toward internet of things.

EXPERIMENTS ON HUMAN SUBJECTS

The evaluation of the sensor was conducted under the approval from the University of Missouri-Columbia Institutional Review Board (project number: 2093707). All human subjects gave written informed consent before participation in the study.

ASSOCIATED CONTENT

Supporting Information

The Supporting Information is available free of charge at https://pubs.acs.org/doi/10.1021/acsanm.4c05362.

https://doi.org/10.1021/acsanm.4c05362
ACS Appl. Nano Mater. 2024, 7, 25241−25248

Comparisons with state-of-the-art LIGs and tactile sensors (Tables S1, S2, S3, and S4); list of acronyms (Table S5); defocus laser and measured laser power output (Figure S1); additional Raman spectra and SEM images (Figures S2, S3, and S4); comparison of LIG defects and their effects on sensor performance (Figure S5); V_{oc} generated from the L60D4 electrode with 0.1 × 0.1 cm (Figure S6); V_{oc} based on the contact with different materials (Figure S7); peak power generated by a single unit of LIG electrodes (Figure S8); and sensor's sensitivity with different silicone thicknesses at the bottom (Figure S9) (PDF)

Video S1: Real-time signals of tactile sensing when wearing the sensor on a human arm (MP4)

Video S2: Real-time data demonstrating the sensor generating precise signal peaks against specific tactile stimuli (MP4)

Video S3: Wirelessly controlling LEDs on/off using touch (MP4)

Video S4: Sliding touch writing a letter "h" mirrored by the LED display (MP4)

AUTHOR INFORMATION

Corresponding Author

Caixia Wan − *Department of Chemical and Biomedical Engineering, University of Missouri, Columbia, Missouri 65211, United States;* orcid.org/0000-0001-5490-7490; Phone: (573) 884-7882; Email: wanca@missouri.edu; Fax: (573) 884-5650

Authors

Shuhong Yang − *Department of Chemical and Biomedical Engineering, University of Missouri, Columbia, Missouri 65211, United States*

Bujingda Zheng − *Department of Mechanical and Aerospace Engineering, University of Missouri, Columbia, Missouri 65211, United States*

Honghua Qian − *Department of Mechanical and Aerospace Engineering, University of Missouri, Columbia, Missouri 65211, United States*

Qiangu Yan − *Forest Products Laboratory, USDA Forest Service, Madison, Wisconsin 53726, United States*

Guoliang Huang − *Department of Mechanical and Aerospace Engineering, University of Missouri, Columbia, Missouri 65211, United States*

Jian Lin − *Department of Mechanical and Aerospace Engineering, University of Missouri, Columbia, Missouri 65211, United States;* orcid.org/0000-0002-4675-2529

Complete contact information is available at: https://pubs.acs.org/10.1021/acsanm.4c05362

Author Contributions

The manuscript was written through contributions of all the authors. The authors have given approval to the final version of the manuscript.

Notes

The authors declare no competing financial interest.

ACKNOWLEDGMENTS

This work was supported by the National Science Foundation (award no. 1933861).

REFERENCES

(1) Le, T. S. D.; Phan, H. P.; Kwon, S.; Park, S.; Jung, Y.; Min, J.; Chun, B. J.; Yoon, H.; Ko, S. H.; Kim, S. W.; et al. Recent advances in laser-induced graphene: mechanism, fabrication, properties, and applications in flexible electronics. *Adv. Funct. Mater.* **2022**, *32* (48), 2205158.

(2) Ye, R.; James, D. K.; Tour, J. M. Laser-induced graphene. *Acc. Chem. Res.* **2018**, *51* (7), 1609−1620.

(3) Ye, R. Q.; Chyan, Y.; Zhang, J. B.; Li, Y. L.; Han, X.; Kittrell, C.; Tour, J. M. Laser-induced graphene formation on wood. *Adv. Mater.* **2017**, *29* (37), 1702211.

(4) Bressi, A. C.; Dallinger, A.; Steksova, Y.; Greco, F. Bio-derived laser-induced graphene for sensors and supercapacitors. *ACS Appl. Mater. Interfaces* **2023**, *15* (30), 35788−35814.

(5) Lin, J.; Peng, Z. W.; Liu, Y. Y.; Ruiz-Zepeda, F.; Ye, R. Q.; Samuel, E. L. G.; Yacaman, M. J.; Yakobson, B. I.; Tour, J. M. Laser-induced porous graphene films from commercial polymers. *Nat. Commun.* **2014**, *5* (1), 5714.

(6) Jayan, J. S.; Jayan, S. S. Biomass-derived laser-induced graphene and its advances in the electronic applications. *Adv. Eng. Mater.* **2023**, *25* (16), 2300248.

(7) Dreimol, C. H.; Guo, H. Z.; Ritter, M.; Keplinger, T.; Ding, Y.; Günther, R.; Poloni, E.; Burgert, I.; Panzarasa, G. Sustainable wood electronics by iron-catalyzed laser-induced graphitization for large-scale applications. *Nat. Commun.* **2022**, *13* (1), 3680.

(8) Mahmood, F.; Zhang, H. W.; Lin, J.; Wan, C. X. Laser-induced graphene derived from kraft lignin for flexible supercapacitors. *ACS Omega* **2020**, *5* (24), 14611−14618.

(9) Lei, Y. J.; Alshareef, A. H.; Zhao, W. L.; Inal, S. Laser-scribed graphene electrodes derived from lignin for biochemical sensing. *ACS Appl. Nano Mater.* **2020**, *3* (2), 1166−1174.

(10) Yang, S. H.; Ling, Y.; Wu, Q.; Zhang, H. W.; Yan, Z.; Huang, G. L.; Lin, J.; Wan, C. X. Lignin-derived porous graphene for wearable and ultrasensitive strain sensors. *J. Mater. Chem. C* **2022**, *10* (32), 11730−11738.

(11) Zhang, H. W.; Sun, Y. S.; Li, Q. W.; Wan, C. X. Upgrading lignocellulose to porous graphene enabled by deep eutectic solvent pretreatment: insights into the role of lignin and pseudo-lignin. *ACS Sustain. Chem. Eng.* **2022**, *10* (35), 11501−11511.

(12) C Claro, P. I.; Pinheiro, T.; Silvestre, S. L.; Marques, A. C.; Coelho, J.; Marconcini, J. M.; Fortunato, E.; C Mattoso, L. H.; Martins, R. Sustainable carbon sources for green laser-induced graphene: a perspective on fundamental principles, applications, and challenges. *Appl. Phys. Rev.* **2022**, *9* (4), 041305.

(13) Meng, L. Y.; Chirtes, S.; Liu, X. J.; Eriksson, M.; Mak, W. C. A green route for lignin-derived graphene electrodes: a disposable platform for electrochemical biosensors. *Biosens. Bioelectron.* **2022**, *218* (3), 114742.

(14) Vinod, A.; Pulikkalparambil, H.; Jagadeesh, P.; Rangappa, S. M.; Siengchin, S. Recent advancements in lignocellulose biomass-based carbon fiber: synthesis, properties, and applications. *Heliyon* **2023**, *9* (3), No. e13614.

(15) Nag, A.; Simorangkir, R. B. V. B.; Gawade, D. R.; Nuthalapati, S.; Buckley, J. L.; O'Flynn, B.; Altinsoy, M. E.; Mukhopadhyay, S. C. Graphene-based wearable temperature sensors: a review. *Mater. Des.* **2022**, *221* (9), 110971.

(16) Peng, Y. Y.; Yang, N.; Xu, Q.; Dai, Y.; Wang, Z. Q. Recent advances in flexible tactile sensors for intelligent systems. *Sensors* **2021**, *21* (16), 5392.

(17) Wang, X. D.; Zhang, Y. F.; Zhang, X. J.; Huo, Z. H.; Li, X. Y.; Que, M. L.; Peng, Z. C.; Wang, H.; Pan, C. F. A highly stretchable transparent self-powered triboelectric tactile sensor with metallized nanofibers for wearable electronics. *Adv. Mater.* **2018**, *30* (12), 1706738.

(18) Yuan, Z. Q.; Shen, G. Z.; Pan, C. F.; Wang, Z. L. Flexible sliding sensor for simultaneous monitoring deformation and displacement on a robotic hand/arm. *Nano Energy* **2020**, *73*, 104764.

(19) Pyo, S.; Lee, J.; Bae, K.; Sim, S.; Kim, J. Recent progress in flexible tactile sensors for human-interactive systems: from sensors to advanced applications. *Adv. Mater.* **2021**, *33* (47), 2005902.

(20) Xu, J. D.; Pan, J.; Cui, T. R.; Zhang, S.; Yang, Y.; Ren, T. L. Recent progress of tactile and force sensors for human-machine interaction. *Sensors* **2023**, *23* (4), 1868.
(21) Ozioko, O.; Navaraj, W.; Hersh, M.; Dahiya, R. Tacsac: A wearable haptic device with capacitive touch-sensing capability for tactile display. *Sensors* **2020**, *20* (17), 4780.
(22) Mandil, W.; Rajendran, V.; Nazari, K.; Ghalamzan-Esfahani, A. Tactile-sensing technologies: trends, challenges and outlook in agri-food manipulation. *Sensors* **2023**, *23* (17), 7362.
(23) Wang, C. F.; Dong, L.; Peng, D. F.; Pan, C. F. Tactile sensors for advanced intelligent systems. *Adv. Intell. Syst.* **2019**, *1* (8), 1900090.
(24) Yun, J.; Jayababu, N.; Kim, D. Self-powered transparent and flexible touchpad based on triboelectricity towards artificial intelligence. *Nano Energy* **2020**, *78*, 105325.
(25) Yang, Y. Q.; Guo, X. G.; Zhu, M. L.; Sun, Z. D.; Zhang, Z. X.; He, T. Y. Y.; Lee, C. K. Triboelectric nanogenerator enabled wearable sensors and electronics for sustainable Internet of Things integrated green earth. *Adv. Energy Mater.* **2023**, *13* (1), 20203040.
(26) Hajra, S.; Panda, S.; Khanberh, H.; Vivekananthan, V.; Chamanehpour, E.; Mishra, Y. K.; Kim, H. J. Revolutionizing self-powered robotic systems with triboelectric nanogenerators. *Nano Energy* **2023**, *115* (4), 108729.
(27) Xu, X. C.; Wu, Q.; Pang, Y. K.; Cao, Y. T.; Fang, Y. H.; Huang, G. L.; Cao, C. Y. Multifunctional metamaterials for energy harvesting and vibration control. *Adv. Funct. Mater.* **2022**, *32* (7), 2107896.
(28) Yeo, J. C.; Lim, C. T. Emerging flexible and wearable physical sensing platforms for healthcare and biomedical applications. *Microsyst. Nanoeng.* **2016**, *2* (1), 16043.
(29) Bajwa, D. S.; Pourhashem, G.; Ullah, A. H.; Bajwa, S. G. A concise review of current lignin production, applications, products and their environmental impact. *Ind. Crop. Prod.* **2019**, *139* (9), 111526.
(30) Chyan, Y.; Ye, R. Q.; Li, Y. L.; Singh, S. P.; Arnusch, C. J.; Tour, J. M. Laser-induced graphene by multiple lasing: toward electronics on cloth, paper, and food. *ACS Nano* **2018**, *12* (3), 2176−2183.
(31) Herziger, F.; Mirzayev, R.; Poliani, E.; Maultzsch, J. *In-situ* Raman study of laser-induced graphene oxidation: In-situ Raman study of laser-induced graphene oxidation. *Phys. Status Solidi B* **2015**, *252* (11), 2451−2455.
(32) Han, X.; Ye, R. Q.; Chyan, Y.; Wang, T.; Zhang, C. H.; Shi, L. L.; Zhang, T.; Zhao, Y.; Tour, J. M. Laser-induced graphene from wood impregnated with metal salts and use in electrocatalysis. *ACS Appl. Nano Mater.* **2018**, *1* (9), 5053−5061.
(33) Kulyk, B.; Silva, B. F. R.; Carvalho, A. F.; Silvestre, S.; Fernandes, A. J. S.; Martins, R.; Fortunato, E.; Costa, F. M. Laser-induced graphene from paper for mechanical sensing. *ACS Appl. Mater. Interfaces* **2021**, *13* (8), 10210−10221.
(34) Zhang, Z. C.; Song, M. M.; Hao, J. X.; Wu, K. B.; Li, C. Y.; Hu, C. G. Visible light laser-induced graphene from phenolic resin: a new approach for directly writing graphene-based electrochemical devices on various substrates. *Carbon* **2018**, *127*, 287−296.
(35) Silvestre, S. L.; Pinheiro, T.; Marques, A. C.; Deuermeier, J.; Coelho, J.; Martins, R.; Pereira, L.; Fortunato, E. Cork derived laser-induced graphene for sustainable green electronics. *Flexible Printed Electron.* **2022**, *7* (3), 035021.
(36) Jahan, N.; Huda, M. M.; Tran, Q. X.; Rai, N. Effect of solvent quality on structure and dynamics of lignin in solution. *J. Phys. Chem. B* **2022**, *126* (31), 5752−5764.
(37) Vermaas, J. V.; Crowley, M. F.; Beckham, G. T. Molecular lignin solubility and structure in organic solvents. *ACS Sustain. Chem. Eng.* **2020**, *8* (48), 17839−17850.
(38) Duval, A.; Vilaplana, F.; Crestini, C.; Lawoko, M. Solvent screening for the fractionation of industrial kraft lignin. *Holzforschung* **2016**, *70* (1), 11−20.
(39) Negishi, R.; Wei, C. P.; Yao, Y.; Ogawa, Y.; Akabori, M.; Kanai, Y.; Matsumoto, K.; Taniyasu, Y.; Kobayashi, Y. Turbostratic stacking effect in multilayer graphene on the electrical transport properties. *Phys. Status Solidi B* **2020**, *257* (2), 1900437.

https://doi.org/10.1021/acsanm.4c05362
ACS Appl. Nano Mater. 2024, 7, 25241−25248